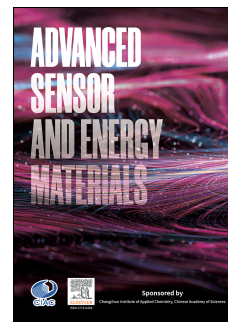


# Journal Pre-proof

Sensitive Detection of SARS-CoV-2 Spike Protein based on Electrochemical Impedance Spectroscopy of Fe<sub>3</sub>O<sub>4</sub>@SiO<sub>2</sub>-Au/GCE Biosensor

Xun-Hai You, Yao Liu, Yan-Yan Li, Bing Zhao, Yong Yang, Rohan Weerasooriya, Xing Chen



PII: S2773-045X(23)00022-5

DOI: <https://doi.org/10.1016/j.asems.2023.100067>

Reference: ASEMS 100067

To appear in: *Advanced Sensor and Energy Materials*

Received Date: 4 May 2023

Revised Date: 23 May 2023

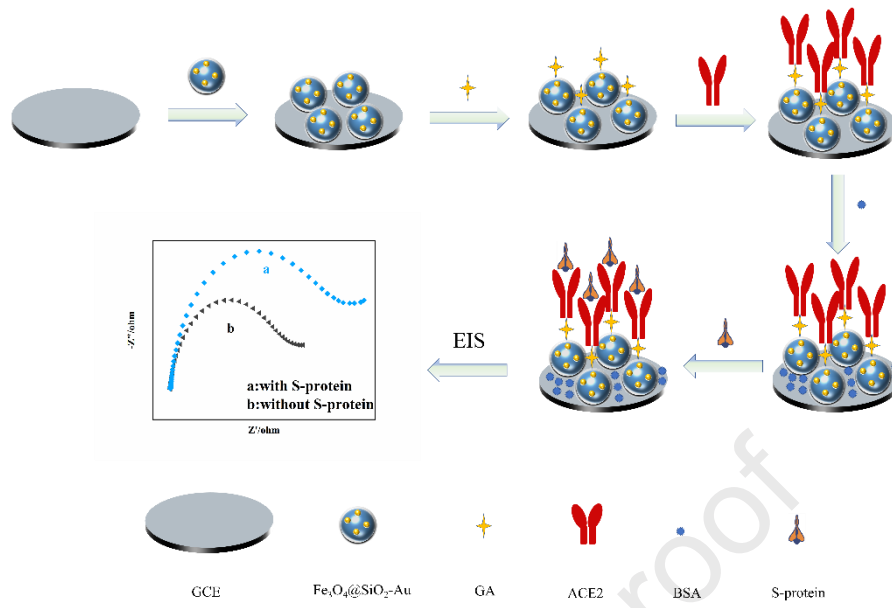
Accepted Date: 24 May 2023

Please cite this article as: X.-H. You, Y. Liu, Y.-Y. Li, B. Zhao, Y. Yang, R. Weerasooriya, X. Chen, Sensitive Detection of SARS-CoV-2 Spike Protein based on Electrochemical Impedance Spectroscopy of Fe<sub>3</sub>O<sub>4</sub>@SiO<sub>2</sub>-Au/GCE Biosensor, *Advanced Sensor and Energy Materials*, <https://doi.org/10.1016/j.asems.2023.100067>.

This is a PDF file of an article that has undergone enhancements after acceptance, such as the addition of a cover page and metadata, and formatting for readability, but it is not yet the definitive version of record. This version will undergo additional copyediting, typesetting and review before it is published in its final form, but we are providing this version to give early visibility of the article. Please note that, during the production process, errors may be discovered which could affect the content, and all legal disclaimers that apply to the journal pertain.

© 2023 The Author(s). Published by Elsevier B.V. on behalf of Changchun Institute of Applied Chemistry, CAS.

Graphical Abstract:



Electrochemical detection of SARS-CoV-2 spike protein based on  $\text{Fe}_3\text{O}_4@\text{SiO}_2\text{-Au}$ /GCE biosensor.

1       **Sensitive Detection of SARS-CoV-2 Spike Protein based on Electrochemical**  
2                   **Impedance Spectroscopy of Fe<sub>3</sub>O<sub>4</sub>@SiO<sub>2</sub>-Au/GCE Biosensor**

3       *Xun-Hai You*<sup>† a, b</sup>, *Yao Liu*<sup>† a, c</sup>, *Yan-Yan Li*<sup>d</sup>, *Bing Zhao*<sup>a, b</sup>, *Yong Yang*<sup>d</sup>, *Rohan*  
4                                   *Weerasooriya*<sup>a, e</sup>, *Xing Chen*<sup>\* a, b, c, e</sup>

5       <sup>a</sup> Key Lab of Aerospace Structural Parts Forming Technology and Equipment of Anhui  
6       Province, Institute of Industry and Equipment Technology, Hefei University of  
7       Technology, Hefei, 230009, P. R. China

8       <sup>b</sup> School of Materials Science and Engineering, Hefei University of Technology, Hefei  
9       230009, P. R. China

10      <sup>c</sup> School of Resources and Environmental Engineering, Hefei University of Technology,  
11      Hefei 230009, P. R. China

12      <sup>d</sup> State Key Laboratory of High-Performance Ceramics and Superfine  
13      Microstructures, Shanghai Institute of Ceramics, Chinese Academy of Sciences,  
14      1295 Dingxi Road, Shanghai 200050, P. R. China

15      <sup>e</sup> National Centre for Water Quality Research, National Institute of Fundamental  
16      Studies, Kandy 20 000, Sri Lanka

17

18

19      † These two authors contributed equally to these work.

20      \* Corresponding author:

21      Xing Chen ([xingchen@hfut.edu.cn](mailto:xingchen@hfut.edu.cn))

22

23

24 **Abstract**

25 Highly contagious COVID-19 disease is caused by a novel severe acute respiratory  
26 syndrome coronavirus 2 (SARS-CoV-2), which poses a serious threat to global public  
27 health. Therefore, the development of a fast and reliable method for the detection of  
28 SARS-CoV-2 is an urgent research need. The Fe<sub>3</sub>O<sub>4</sub>@SiO<sub>2</sub>-Au is enriched with a  
29 variety of functional groups, which can be used to fabricate a sensitive electrochemical  
30 biosensor by biofunctionalization with angiotensin-converting enzyme 2 (ACE2).  
31 Accordingly, we developed a novel electrochemical sensor by chemically modifying a  
32 glassy carbon electrode (GCE) with Fe<sub>3</sub>O<sub>4</sub>@SiO<sub>2</sub>-Au nanocomposites (hereafter  
33 Fe<sub>3</sub>O<sub>4</sub>@SiO<sub>2</sub>-Au/GCE) for the rapid detection of S-protein spiked SARS-CoV-2 by  
34 electrochemical impedance spectroscopy (EIS). The new electrochemical sensor has a  
35 low limit detection (viz., 4.78 pg/mL) and a wide linear dynamic range (viz., 0.1 ng/mL  
36 to 10 µg/mL) for detecting the EIS response signal of S-protein. The robust  
37 Fe<sub>3</sub>O<sub>4</sub>@SiO<sub>2</sub>-Au/GCE biosensor has high selectivity, stability, and reproducibility for  
38 the detection of S-protein with good recovery of saliva samples.

39 **Keywords:** SARS-CoV-2 spike protein, Fe<sub>3</sub>O<sub>4</sub>@SiO<sub>2</sub>-Au nanocomposites,  
40 electrochemical biosensor, electrochemical impedance spectroscopy

41

## 42 **Introduction**

43        Since the 21st century, three coronavirus outbreaks were reported at a global scale:  
44 severe acute respiratory syndrome (SARS) in 2002, Middle East respiratory syndrome  
45 (MERS) in 2012, and novel pneumonia caused by a coronavirus (SARS-CoV-2) in 2019  
46 Corona Virus Disease 2019 (COVID-19) [1, 2]. It is reported that the SARS-CoV-2  
47 genome sequence is 77% and 50% homologous to SARS-CoV and MERS-CoV,  
48 respectively [3]. SARS-CoV-2 is more widespread compared to the other respiratory  
49 syndromes by spreading over two hundred countries causing 600 million infections and  
50 about 6 million deaths. Therefore, the development of a rapid and sensitive method for  
51 the detection of SARS-CoV-2 is urgently needed. Currently, virus detection methods  
52 rely on conventional laboratory techniques, including nucleic acid detection and  
53 serological testing [4-6]. Among nucleic acid assay routes, the reverse transcription  
54 polymerase chain reaction (RT-PCR) is the core method for SARS-CoV-2 detection.  
55 However, RT-PCR-based methods require skilled personnel and specialized equipment  
56 [7]. Serological assays viz., including antigen and antibody assays, are based on  
57 antigen-antibody-specific binding assays [8, 9]. There is a voluminous literature on the  
58 benefits of serological assays for SARS-CoV-2 detection, where antigen assays can  
59 only be used adjunct to detect SARS-CoV-2 [10]. Although these methods consume  
60 less time than RT-PCR measurements, they still have limitations due to arduous sample  
61 preparations and low sensitivity. Further the production of antibody assays requires  
62 SARS-CoV-2 infected patients for a period of 5 to 7 days. Previously, the development  
63 of electrochemical biosensors for medical diagnostic applications [11-13], including  
64 diabetes, Alzheimer's, and other diseases, have shown that they can be adapted as a viral  
65 detection tool with high sensitivity, high specificity, low cost, and fast response time  
66 (Table. S1). Notably, with the miniaturization and smart automation of electrochemical

67 devices, these biosensors are also suited for clinical diagnosis and rapid detection of  
68 SARS-CoV-2 [14-16].

69 One of the key aspects of constructing electrochemical biosensors is the  
70 development of stable materials with desired conductivity and selectivity to an analyte  
71 [17, 18]. There is a considerable literature on the development of different  
72 nanomaterials in electrochemical biosensors [19-22], including gold, carbon, metal  
73 oxide nanomaterials, etc. Fe<sub>3</sub>O<sub>4</sub> nanoparticles attract attention in electrochemical sensor  
74 development particularly due to their biocompatibility, simple preparation, magnetic  
75 properties, high sorption capacity, and environmentally benign nature [23]. However,  
76 iron-derived substrates readily agglomerate and undergo rapid oxidation which limits  
77 their efficient use in sensor developments [24, 25]. To overcome these limitations and  
78 enhance stability, Fe<sub>3</sub>O<sub>4</sub> nanoparticles are suitably compounded with carbon-derived  
79 substrates, metal oxides, and other metals, or polymers, etc. [23] Presently, we  
80 developed a sensor by modifying glassy carbon electrode (GCE) with Fe<sub>3</sub>O<sub>4</sub>@SiO<sub>2</sub>-Au  
81 nanocomposites to detect S-protein for SARS-CoV-2 diagnosis by electrochemical  
82 impedance spectroscopy (EIS). To facilitate electron transfer, minimize agglomeration,  
83 and retard undesired oxidation, the Fe<sub>3</sub>O<sub>4</sub> nanoparticles were first coated with a thin  
84 SiO<sub>2</sub> layer and then doped with Au nanoparticles. To improve selectivity and sensitivity  
85 of SARS-CoV-2 detection, angiotensin-converting enzyme 2 (ACE2) was introduced  
86 to functionalize Fe<sub>3</sub>O<sub>4</sub>@SiO<sub>2</sub>-Au composite to enhance S-protein binding ability [26-  
87 29]. This enables the rapid diagnosis of SARS-CoV-2 virus, which may open a new  
88 direction in COVID-19 research.

89

## 90 **2. Materials and methods**

### 91 *2.1. Materials and apparatus*

92 The SARS-CoV-2 S-protein and Fc-tag-tagged human ACE2 were obtained from  
93 Sino Biological (PR China). Analytical grade, ferric chloride hexahydrate  
94 ( $\text{FeCl}_3 \cdot 6\text{H}_2\text{O}$ ), ethylene glycol ( $\text{C}_2\text{H}_6\text{O}_2$ ), trisodium citrate dihydrate  
95 ( $\text{C}_6\text{H}_5\text{Na}_3\text{O}_7 \cdot 2\text{H}_2\text{O}$ ), sodium acetate anhydrous ( $\text{CH}_3\text{COONa}$ ), tetraethyl orthosilicate  
96 (TEOS), ammonia, 3-aminopropyl-triethoxysilane (APTES), chloroauric acid  
97 ( $\text{HAuCl}_4 \cdot 4\text{H}_2\text{O}$ ), ethanol, potassium dihydrogen phosphate ( $\text{KH}_2\text{PO}_4$ ), disodium  
98 hydrogen phosphate ( $\text{Na}_2\text{HPO}_4 \cdot 12\text{H}_2\text{O}$ ), glutaraldehyde (GA), glucose, ascorbic acid,  
99 norfloxacin, uric acid, tenofovir, favipiravir, histidine, oxytetracycline were purchased  
100 from Sinopharm Chemical Reagent Co., Ltd (PR China) and used as received. Human  
101 IgG and bovine serum albumin (BSA) were purchased from Dingguo Changsheng  
102 Biotechnology Limited Company (PR China). The real saliva samples were collected  
103 from the Hefei University of Technology Hospital. Ultra-high pure water (conductivity  
104  $0.0548 \mu\text{S}/\text{cm}$ ) was used in laboratory preparations.

105 High-resolution scanning electron microscopy (HRSEM) images of the samples  
106 were obtained by Regulus 8230 at an operating voltage of 15 kV (Hitachi Ltd., Japan).  
107 Transmission electron microscopy (TEM) micrographs were recorded on JEM-  
108 1400FLASH (JEOL, Japan). X-ray diffraction (XRD) patterns of the samples were  
109 recorded by Xpert PRO MPD (Nalytical, Netherlands). Magnetic measurement was  
110 carried out using an MPMS 3 vibrating sample magnetometer (Quantum Design, USA).  
111 The fourier-transform infrared spectroscopy (FTIR) technique was carried out using a  
112 Nicolet IS50 iN10 instrument (Thermo Nicolet, USA). Zeta potential was carried out  
113 using a Zetasizer Nano ZS-90 (Spectris, China). X-ray photoelectron spectroscopy  
114 (XPS) technique was used with an EscaLab 250Xi instrument (Thermo, USA).

115

116 *2.2 Preparation of  $\text{Fe}_3\text{O}_4@\text{SiO}_2\text{-Au}$  nanomaterials*

### 117 2.2.1 Synthesis of $Fe_3O_4$ nanoparticles

118 The  $Fe_3O_4$  nanoparticles were synthesized as described in Liu [30] with the  
119 following modifications. 2.025 g  $FeCl_3 \cdot 6H_2O$  was dissolved in 60 mL ethylene glycol  
120 with stirring for 30 min, then 0.88 g  $C_6H_5Na_3O_7 \cdot 2H_2O$  was added and heated to  $60^\circ C$   
121 with stirring continued for 30 min. Finally, 9.84 g  $CH_3COONa$  were added to provide  
122 alkaline conditions enabling complete dissolution of the substrate. The dark yellow  
123 solution thus received was transferred to PTFE lined stainless-steel sealed container  
124 and autoclaved at  $180^\circ C$  for 8 h. After cooling to room temperature, the substrate ( $Fe_3O_4$ )  
125 was magnetically separated and washed with ethanol and deionized water for three  
126 times each, then vacuum dried at  $60^\circ C$ .

127

### 128 2.2.2 Synthesis of $Fe_3O_4@SiO_2$ nanocomposites

129 Using the Stöber improvement method [31], 0.05 g  $Fe_3O_4$  nanoparticles were  
130 dissolved in a mixture of ethanol (80 mL) and deionized water (16 mL), sonicated for  
131 20 min. Subsequently, to this mixture ammonia solution (2 mL, 28wt%) was added  
132 followed by the slow addition of TEOS (1 mL) and was kept stirring at room  
133 temperature for 6 h. The resultant substrate was magnetically recovered and washed  
134 with ethanol and deionized for three times each, then vacuum dried at  $60^\circ C$  to yield  
135  $Fe_3O_4@SiO_2$  nanocomposites.

136

### 137 2.2.3 Preparation of Au nanoparticles

138 Au nanoparticles were obtained by reducing  $HAuCl_4 \cdot 4H_2O$  with sodium citrate  
139 [32]. Briefly,  $HAuCl_4 \cdot 4H_2O$  (100 mL, 1wt %) aqueous solution was heated at  $100^\circ C$   
140 and 10 mL 38.8 mmol/L  $C_6H_5Na_3O_7 \cdot 2H_2O$  was added into the stirred solution when it  
141 started boiling. Finally, the dark brown colored Au nanoparticles were obtained.

142

143 *2.2.4 Synthesis of Fe<sub>3</sub>O<sub>4</sub>@SiO<sub>2</sub>-Au nanocomposites*

144 To functionalize Fe<sub>3</sub>O<sub>4</sub>@SiO<sub>2</sub> with -NH<sub>2</sub> groups, 0.1 g Fe<sub>3</sub>O<sub>4</sub>@SiO<sub>2</sub> was dispersed  
145 in ethanol (47.5 mL) and deionized water (2.5 mL) mixture followed by the addition of  
146 0.4 mL APTES into the suspension with stirring for 4 h (Fe<sub>3</sub>O<sub>4</sub>@SiO<sub>2</sub>-NH<sub>2</sub>). The  
147 Fe<sub>3</sub>O<sub>4</sub>@SiO<sub>2</sub>-NH<sub>2</sub> was re-dissolved in 40 mL deionized water, and then a certain  
148 amount of Au nanoparticles was added with stirring for 4 h. The resultant nanoparticles  
149 were magnetically separated and washed three times with ethanol and deionized water,  
150 then vacuum dried at 60°C. In addition, the Au nanoparticles loading on Fe<sub>3</sub>O<sub>4</sub>@SiO<sub>2</sub>  
151 composite were varied between 5 mL, 15 mL and 25 mL Au nanoparticles solution  
152 (hereafter designated as Fe<sub>3</sub>O<sub>4</sub>@SiO<sub>2</sub>-Au<sub>x</sub> where x = 1,2,3). Without special instructions,  
153 Fe<sub>3</sub>O<sub>4</sub>@SiO<sub>2</sub>-Au nanocomposites synthesized from 15 mL Au nanoparticles were  
154 applied in the subsequent experiments.

155

156 *2.3 Fabrication of S-protein electrochemical biosensor*

157 The fabrication methodology of the chemically modified glassy carbon electrode  
158 (GCE) used for SARS-CoV-2 S-protein detection is shown in Scheme 1. The GCE was  
159 polished to a mirror surface using alumina powder with decreasing particle sizes: 1.0  
160 μm, 0.3 μm, and 0.05 μm. Then the GCEs were ultrasonically cleaned with ethanol and  
161 ultrapure water for 3 min. Afterward, 6 μL of 3 mg/mL Fe<sub>3</sub>O<sub>4</sub>@SiO<sub>2</sub>-Au suspension  
162 was added dropwise onto the electrode surface to obtain a chemically modified  
163 electrode, e.g., Fe<sub>3</sub>O<sub>4</sub>@SiO<sub>2</sub>-Au/GCE. The Fe<sub>3</sub>O<sub>4</sub>@SiO<sub>2</sub>-Au/GCE was then

164 functionalized using glutaraldehyde (GA), ACE2, and bovine serum albumin (BSA).  
165 To modify with ACE2, the Fe<sub>3</sub>O<sub>4</sub>@SiO<sub>2</sub>-Au/GCE surface was first functionalized with  
166 GA, then the receptor protein ACE2 was attached to the electrode surface at room  
167 temperature. Subsequently, the electrode surface was incubated using BSA prepared to  
168 block the possible binding sites of GA on the electrode surface  
169 (BSA/ACE2/GA/Fe<sub>3</sub>O<sub>4</sub>@SiO<sub>2</sub>-Au/GCE).

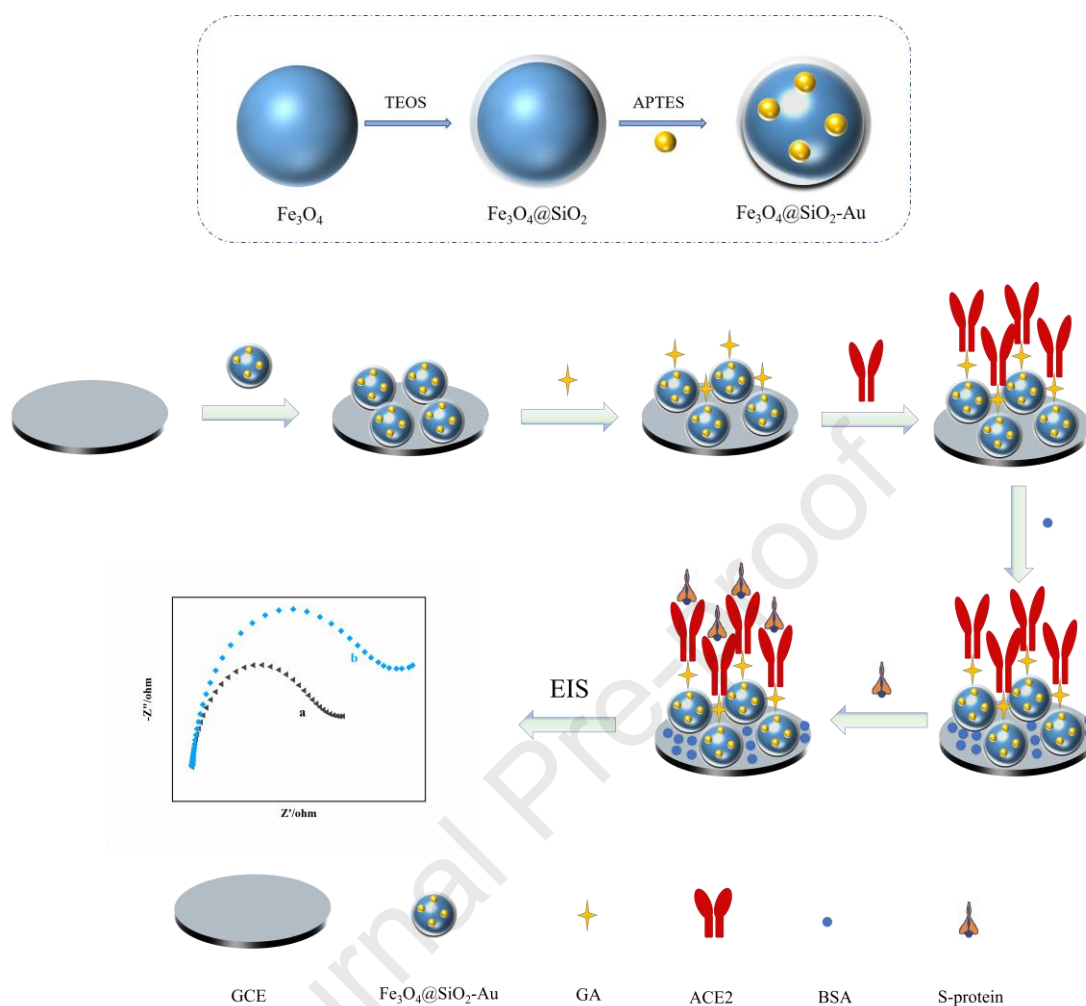
170

#### 171 *2.4 Characterizations of S-protein electrochemical biosensor*

172 The binding of SARS-CoV-2 S-protein onto the electrochemical biosensor was  
173 attained by adding 6 µL S-protein solution on the BSA/ACE2/GA/Fe<sub>3</sub>O<sub>4</sub>@SiO<sub>2</sub>-  
174 Au/GCE surface and incubating at 37°C for 30 min. The cyclic voltammetry (CV)  
175 curves and electrochemical impedance spectrograms (EIS) were obtained by a three-  
176 electrode configuration, viz. chemically modified GCE, Ag/AgCl reference, and Pt  
177 counter electrodes, using 5.0 mmol/L [Fe(CN)<sub>6</sub>]<sup>3-/4-</sup> in 0.1 mol/L PBS with a pH 7.0  
178 (Electrochemical station, CHI760E, China). The scan rate of the electrochemical  
179 analyzer was set at 100 mV/s in the CV experiments; EIS measurements were carried  
180 out in a frequency range of 0.1 Hz to 100 kHz, with a signal amplitude (< 10 mV) and  
181 open-circuit potential of 0.33 V. All experiments were performed at room temperature.  
182 The electrochemical impedance data was modeled with modified equivalent circuits  
183 using ZView software to estimate the charge transfer resistance under different  
184 experimental conditions. Finally, an electroanalytical method was developed based on  
185 EIS for S-protein detection using the newly developed chemically modified  
186 Fe<sub>3</sub>O<sub>4</sub>@SiO<sub>2</sub>-Au electrode.

187

188



189

190 Scheme 1. Schematic illustration of the preparation process for  $\text{Fe}_3\text{O}_4@\text{SiO}_2\text{-Au}$  and  
 191 the fabrication of the electrochemical biosensor.

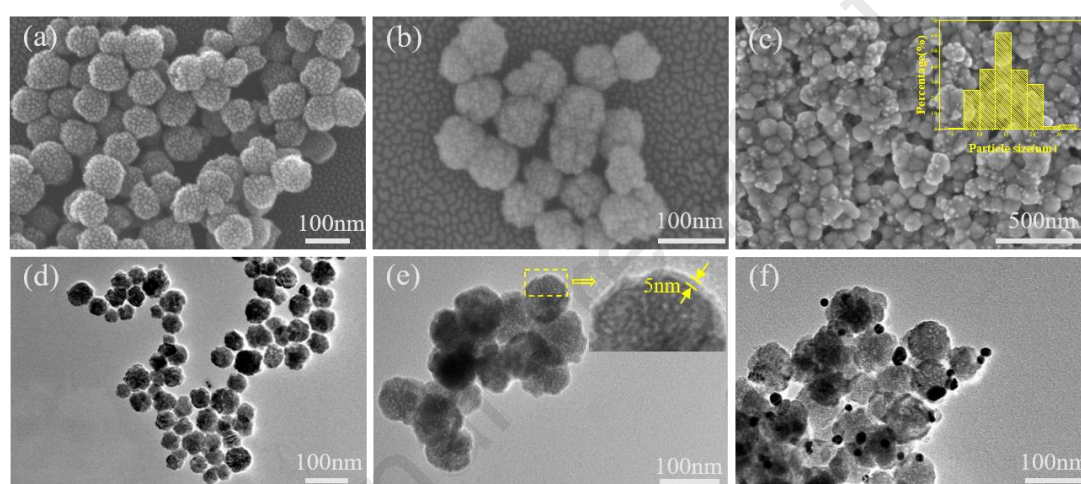
192

### 193 3. Results and discussion

#### 194 3.1 Physical and chemical characterizations of the $\text{Fe}_3\text{O}_4@\text{SiO}_2\text{-Au}$ nanocomposite

195 Fig. 1 shows the morphology and micro-structures of  $\text{Fe}_3\text{O}_4$ ,  $\text{Fe}_3\text{O}_4@\text{SiO}_2$ , and  
 196  $\text{Fe}_3\text{O}_4@\text{SiO}_2\text{-Au}$  nanomaterials observed through HRSEM and TEM.  $\text{Fe}_3\text{O}_4$   
 197 particulates tend to coagulate readily and citrate ligand was used to minimize  
 198 coagulation [33]. As shown in Figs. 1a & d,  $\text{Fe}_3\text{O}_4$  particulates are well-dispersed and  
 199 spherical around the 60 to 70 nm size range. However, as shown in Fig. 1b, the

200  $\text{Fe}_3\text{O}_4@\text{SiO}_2$  nanocomposites are not well resolved to observe  $\text{SiO}_2$  coating around  
 201  $\text{Fe}_3\text{O}_4$  (except for some tonal variations). Therefore, the  $\text{SiO}_2$  coating around the  $\text{Fe}_3\text{O}_4$   
 202 forming a core-shell structure is shown in TEM analysis. The thickness of the  $\text{SiO}_2$   
 203 layer is around 5 nm (Fig. 1e). The spread of Au nanoparticles around 15 nm average  
 204 size on  $\text{Fe}_3\text{O}_4@\text{SiO}_2$  surface is visible in both SEM and TEM images. As shown in Figs.  
 205 1c & f, the Au nanoparticles are well-spread on the  $\text{Fe}_3\text{O}_4@\text{SiO}_2$  surface forming a large  
 206 proportion of active sites to sequester ACE2 receptor protein.

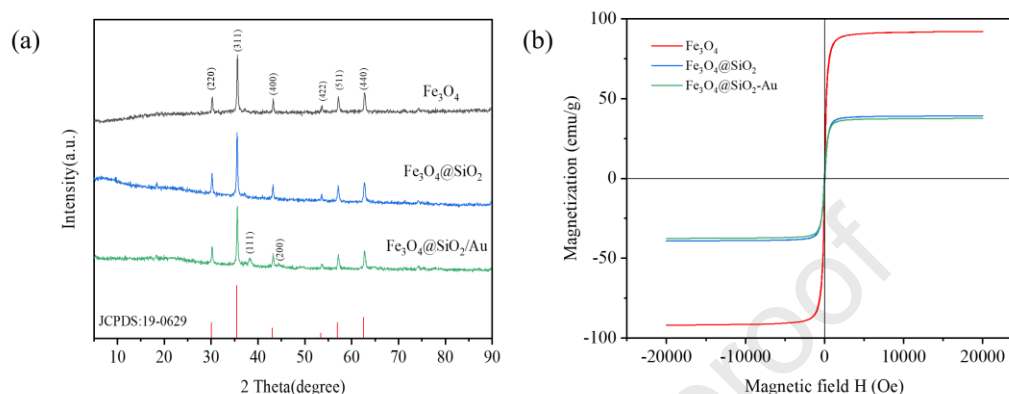


207

208 Fig. 1. Morphological characterization of nanomaterials: HRSEM images of (a)  $\text{Fe}_3\text{O}_4$ ,  
 209 (b)  $\text{Fe}_3\text{O}_4@\text{SiO}_2$ , (c)  $\text{Fe}_3\text{O}_4@\text{SiO}_2\text{-Au}$ , TEM images of (d)  $\text{Fe}_3\text{O}_4$ , (e)  $\text{Fe}_3\text{O}_4@\text{SiO}_2$ , (f)  
 210  $\text{Fe}_3\text{O}_4@\text{SiO}_2\text{-Au}$ .

211 The XRD diffractograms of  $\text{Fe}_3\text{O}_4$ ,  $\text{Fe}_3\text{O}_4@\text{SiO}_2$ , and  $\text{Fe}_3\text{O}_4@\text{SiO}_2\text{-Au}$   
 212 nanomaterials are shown in Fig. 2a. The X-ray diffraction peaks of  $\text{Fe}_3\text{O}_4$  at  $2\theta$  of  $30.2^\circ$ ,  
 213  $35.6^\circ$ ,  $43.2^\circ$ ,  $53.6^\circ$ ,  $57.2^\circ$ , and  $62.7^\circ$ , respectively are in agreement with spinel structure  
 214 corresponding to (220), (311), (400), (422), (511), and (440) lattice planes (JCPDF:19-  
 215 0629) [34, 35]. In addition, the intensity of these diffraction peaks and the standard  
 216 patterns are almost the same, indicating good  $\text{Fe}_3\text{O}_4$  crystallinity. Further, the X-ray  
 217 diffractograms of  $\text{Fe}_3\text{O}_4@\text{SiO}_2$  and  $\text{Fe}_3\text{O}_4$  are also similar due to the amorphous nature  
 218 of  $\text{SiO}_2$  coating. The XRD data of  $\text{Fe}_3\text{O}_4@\text{SiO}_2\text{-Au}$  show the presence of  $\text{Fe}_3\text{O}_4$  along

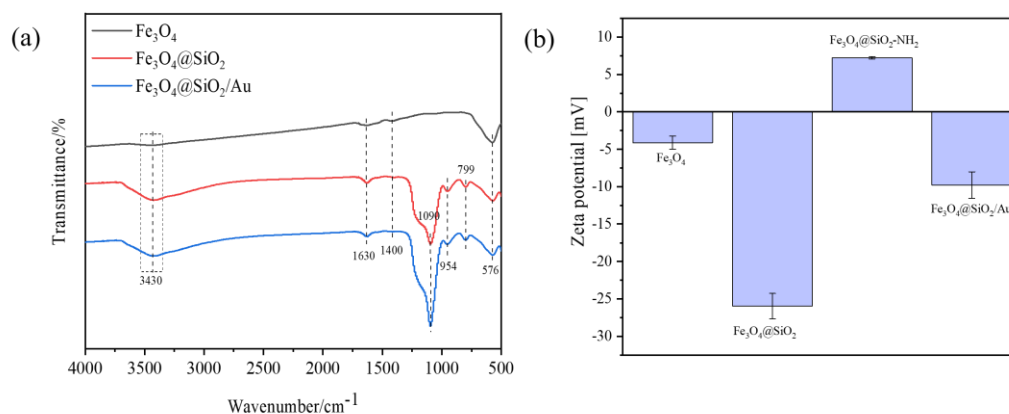
219 (111) and (200) lattice planes of cubic Au nanoparticles corresponding to  $2\theta$  at  $38.2^\circ$   
 220 and  $44.4^\circ$ . The experimental data confirms further the successful incorporation of Au  
 221 cubic nanocrystals on  $\text{Fe}_3\text{O}_4@\text{SiO}_2$  composites (hereafter  $\text{Fe}_3\text{O}_4@\text{SiO}_2\text{-Au}$ ).



222

223 Fig. 2. (a) The XRD patterns and (b) magnetic hysteresis loops of  $\text{Fe}_3\text{O}_4$ ,  $\text{Fe}_3\text{O}_4@\text{SiO}_2$ ,  
 224  $\text{Fe}_3\text{O}_4@\text{SiO}_2\text{-Au}$ .

225 The magnetic properties of  $\text{Fe}_3\text{O}_4$ ,  $\text{Fe}_3\text{O}_4@\text{SiO}_2$ , and  $\text{Fe}_3\text{O}_4@\text{SiO}_2\text{-Au}$   
 226 nanomaterials are shown in Fig. 2b. The remanence and coercivity of material show  
 227 their resistivity to demagnetization. Presently, all our nanomaterials observed zero  
 228 remanence and coercivity values confirming their super magnetic properties. The B-H  
 229 curves of  $\text{Fe}_3\text{O}_4@\text{SiO}_2$  and  $\text{Fe}_3\text{O}_4@\text{SiO}_2\text{-Au}$  are almost overlapped showing that the  
 230 Au addition did not appreciably alter the magnetic strength of the composite. The  
 231 magnetization intensity of  $\text{Fe}_3\text{O}_4$  nanoparticles decreased from  $87.67 \text{ emu/g}$  to  $39.18$   
 232  $\text{ emu/g}$  and  $37.61 \text{ emu/g}$  upon sequential cladding with  $\text{SiO}_2$  and Au doping, which  
 233 confirms the successful synthesis of  $\text{Fe}_3\text{O}_4@\text{SiO}_2\text{-Au}$ .



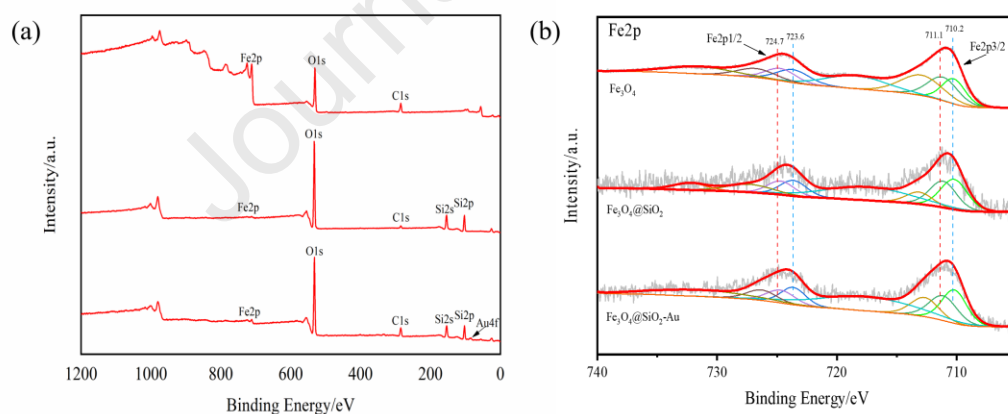
234

235 Fig. 3. (a) The FTIR spectra of Fe<sub>3</sub>O<sub>4</sub>, Fe<sub>3</sub>O<sub>4</sub>@SiO<sub>2</sub>, Fe<sub>3</sub>O<sub>4</sub>@SiO<sub>2</sub>-Au. (b) The Dynamic  
 236 Light Scattering (DLS, Zeta potentials) of Fe<sub>3</sub>O<sub>4</sub>, Fe<sub>3</sub>O<sub>4</sub>@SiO<sub>2</sub>, Fe<sub>3</sub>O<sub>4</sub>@SiO<sub>2</sub>-NH<sub>2</sub>,  
 237 Fe<sub>3</sub>O<sub>4</sub>@SiO<sub>2</sub>-Au.

238 The FTIR spectra of Fe<sub>3</sub>O<sub>4</sub>, Fe<sub>3</sub>O<sub>4</sub>@SiO<sub>2</sub>, and Fe<sub>3</sub>O<sub>4</sub>@SiO<sub>2</sub>-Au nanomaterials are  
 239 shown in Fig. 3.a. The characteristic peaks detected at 1630 cm<sup>-1</sup> and 3430 cm<sup>-1</sup> are  
 240 attributed to the stretching vibration of -OH, while the 799 cm<sup>-1</sup> and 1090 cm<sup>-1</sup> are  
 241 ascribed due to Si-O stretching vibrations (this band is absent in Fe<sub>3</sub>O<sub>4</sub>). The IR bands  
 242 at 576 cm<sup>-1</sup> and 1400 cm<sup>-1</sup> are specific to the stretching of Fe-O and -COOH,  
 243 respectively [36]. Interestingly, the IR intensity of Fe-O bands decreases as Fe<sub>3</sub>O<sub>4</sub> >  
 244 Fe<sub>3</sub>O<sub>4</sub>@SiO<sub>2</sub> > Fe<sub>3</sub>O<sub>4</sub>@SiO<sub>2</sub>-Au, which may be related to the coating of SiO<sub>2</sub> and  
 245 doping of Au nanoparticles. Fig. 3b shows the zeta potential values of Fe<sub>3</sub>O<sub>4</sub>,  
 246 Fe<sub>3</sub>O<sub>4</sub>@SiO<sub>2</sub>, and Fe<sub>3</sub>O<sub>4</sub>@SiO<sub>2</sub>-Au suspensions measured in pH 7.0. Bare Fe<sub>3</sub>O<sub>4</sub>  
 247 nanoparticles show a -4.11mV zeta potential. After incorporating SiO<sub>2</sub> onto Fe<sub>3</sub>O<sub>4</sub>  
 248 nanoparticles, the surface becomes negatively charged due to the abundance of -OH  
 249 offsets Fe-O charging. The negative zeta potential values show little agglomeration of  
 250 Fe<sub>3</sub>O<sub>4</sub>@SiO<sub>2</sub> nanocomposites. When APTES is used to functionalize Fe<sub>3</sub>O<sub>4</sub>@SiO<sub>2</sub> sites  
 251 a surface charge reversal occurred confirming the grafting of positively charged amino  
 252 groups to the terminus of the substrates (viz., Fe<sub>3</sub>O<sub>4</sub>@SiO<sub>2</sub>-NH<sub>2</sub>). The positively  
 253 charged Fe<sub>3</sub>O<sub>4</sub>@SiO<sub>2</sub>-NH<sub>2</sub> sites adhere to Au nanoparticles readily again reversing the

254 surface charge [37]. According to IR and zeta potential data, the -OH, -COOH, and -  
 255 NH<sub>2</sub> groups abut from the Fe<sub>3</sub>O<sub>4</sub>@SiO<sub>2</sub>-Au surface favor intimate interactions with  
 256 receptor protein ACE2.

257 Fig. 4a shows the XPS survey spectra Fe<sub>3</sub>O<sub>4</sub>, Fe<sub>3</sub>O<sub>4</sub>@SiO<sub>2</sub>, Fe<sub>3</sub>O<sub>4</sub>@SiO<sub>2</sub>-Au  
 258 nanomaterials, the presence of Fe, Si, Au, and associate valence states are confirmed.  
 259 As shown in Fig. 4b, in all samples the deconvoluted peaks at 710.2 eV (Fe2p1/2) and  
 260 723.6 eV (Fe2p2/3) with a satellite confirming the presence of Fe<sup>2+</sup>. Similarly, the peaks  
 261 at 711.1eV and 724.67 eV and the satellite show Fe<sup>3+</sup> [38, 39]. Moreover, the signatures  
 262 of Fe2p peaks do not vary which verifies the presence of Fe<sup>2+</sup> and Fe<sup>3+</sup> states [38, 39].  
 263 The positions of the prominent Fe2p peaks of the three substrates magnetic did not shift,  
 264 which verifies that all Fe<sup>2+</sup> and Fe<sup>3+</sup> in all samples. As the XPS analysis was within 5nm  
 265 depth of the sample surface, the fluctuation of Fe2p peaks during cladding and doping  
 266 may be wide.



267  
 268 Fig. 4. (a) XPS full spectrum of Fe<sub>3</sub>O<sub>4</sub>@SiO<sub>2</sub>-Au materials. (b) Fe2p energy spectrum  
 269 of Fe<sub>3</sub>O<sub>4</sub>, Fe<sub>3</sub>O<sub>4</sub>@SiO<sub>2</sub>, and Fe<sub>3</sub>O<sub>4</sub>@SiO<sub>2</sub>-Au

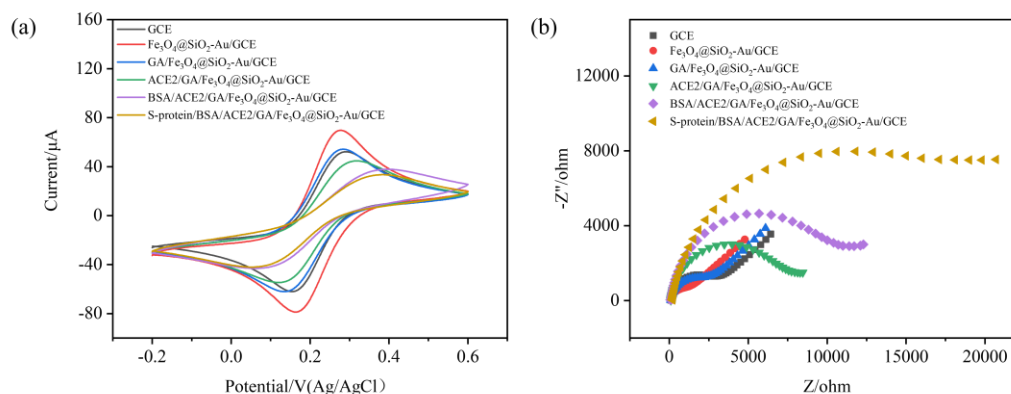
270 Fig. S1 shows the stability tests of three nanomaterials, confirming the  
 271 contribution of SiO<sub>2</sub> coating to the stability of the nanocomposite coatings by  
 272 comparing the changes in the redox peak currents of Fe<sub>3</sub>O<sub>4</sub>, Fe<sub>3</sub>O<sub>4</sub>@SiO<sub>2</sub>, and

273  $\text{Fe}_3\text{O}_4@\text{SiO}_2\text{-Au}$  nanomaterials. The results conclude that  $\text{Fe}_3\text{O}_4@\text{SiO}_2\text{-Au}$  modified  
274 GCE is robust to the fabrication biosensor. Also shown in Fig. S1g & h, the oxidation  
275 peak current of the  $\text{Fe}_3\text{O}_4@\text{SiO}_2\text{-Au}$  nanomaterials modified electrode was reduced by  
276 9.2% from day 1 to day 14. Therefore, all electrochemical biosensor data presented in  
277 this study were obtained using the newly modified electrode.

278 The cyclic voltametric curves (CV) obtained for 5.0 mmol/L  $[\text{Fe}(\text{CN})_6]^{3-/4-}$  in 0.1  
279 mol/L PBS at pH 7.0 using bare and chemically modified GCE sensors are shown in  
280 Fig. S2. Always the CV curves show a symmetry due to the reversible nature of  $\text{Fe}^{2+} \rightarrow$   
281  $\text{Fe}^{3+}$  electron transfer. The highest CV current peak is observed with  $\text{Fe}_3\text{O}_4@\text{SiO}_2\text{-}$   
282  $\text{Au/GCE}$  sensor due to the presence of Au nanoparticles (Fig. S2a). The current peak  
283 values decrease in order  $\text{Fe}_3\text{O}_4@\text{SiO}_2\text{-Au/GCE} > \text{Fe}_3\text{O}_4/\text{GCE} > \text{Fe}_3\text{O}_4@\text{SiO}_2/\text{GCE} >$   
284 bare GCE showing the hindrance for electrons transfer due to the presence of  $\text{SiO}_2$ . Fig.  
285 S2b shows the calibration curve to the peak current intensity with the square root of the  
286 scanning rate recorded for different nanomaterial-modified electrodes. The calculated  
287 electrochemically active surface area of bare GCE,  $\text{Fe}_3\text{O}_4/\text{GCE}$ ,  $\text{Fe}_3\text{O}_4@\text{SiO}_2/\text{GCE}$ , and  
288  $\text{Fe}_3\text{O}_4@\text{SiO}_2\text{-Au/GCE}$  obtained by Randles-Sevcik formula[40] is 0.043  $\text{cm}^2$ , 0.055  
289  $\text{cm}^2$ , 0.051  $\text{cm}^2$  and 0.060  $\text{cm}^2$ , respectively. The high electron transport capacity of  
290  $\text{Fe}_3\text{O}_4$  nanoparticles and Au nanoparticles can increase the electrochemically active area  
291 of the modified electrode, providing more electrochemically active sites for receptor  
292 protein ACE2 immobilization.

293

294 *3.2 The electrochemical characterization of the biosensors*



295

296 Fig. 5. The cyclic voltammograms (a) and Nyquist plots (b) representing the stepwise  
 297 deposition of  $\text{Fe}_3\text{O}_4@\text{SiO}_2\text{-Au}$  nanomaterials, glutaraldehyde (GA), receptor protein  
 298 ACE2, bovine serum albumin (BSA) blocker, and 0.1 ng/mL SARS-CoV-2 S-protein.

299 The as-fabricated electrochemical biosensor process was elucidated by CV and  
 300 EIS in 5.0 mmol/L  $[\text{Fe}(\text{CN})_6]^{3-/4-}$  in 0.1 mol/L PBS with a pH 7.0. As shown in Fig. 5a,  
 301 after the modification of GCE by the  $\text{Fe}_3\text{O}_4@\text{SiO}_2\text{-Au}$ , the value of the redox current  
 302 dramatically augmented compared to the GCE. This is due to the good electrochemical  
 303 activity of  $\text{Fe}_3\text{O}_4@\text{SiO}_2\text{-Au}$  which accelerates the electron transfer on the electrode  
 304 surface. When GA and the receptor protein ACE2 are immobilized on the modified  
 305 electrode surface, the redox current significantly decreased due to the presence  
 306 of cross-linked macromolecular structures in GA and the receptor protein ACE2, which  
 307 prevented electron transfer. Moreover, when the BSA was used to block the non-  
 308 specific active sites, the redox peak further decreased. The lowest redox peak for the S-  
 309 protein was attributed to the tight binding of the S-protein and the receptor protein  
 310 ACE2, which made the exchange reaction between electrons at the electrode surface  
 311 more difficult. Fig. 5b shows Nyquist plots including semicircle (a measure of electron  
 312 transfer rate) and linear (a measure of charge diffusion) segments representing high and

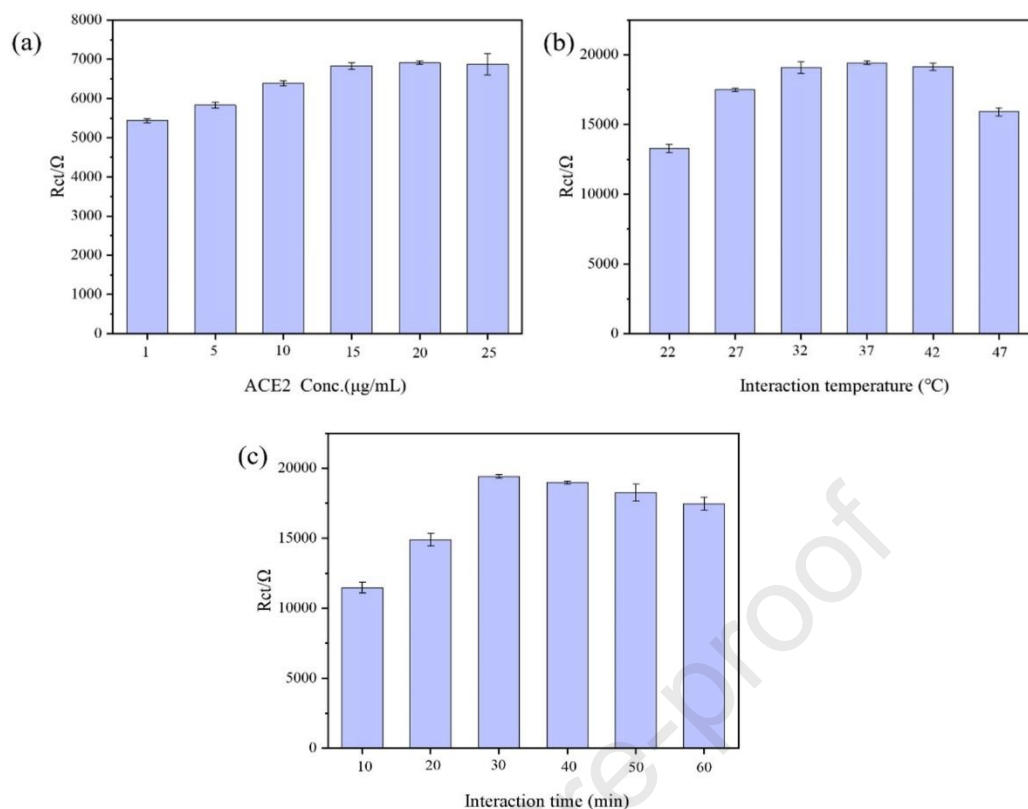
313 low-frequency regions [41-43]. The EIS measurements are in agreement with the CV  
314 data. The  $\text{Fe}_3\text{O}_4@\text{SiO}_2\text{-Au}$  modified GCE had the smallest charge-transfer resistance  
315 ( $R_{ct}$ ) compared to the bare GCE. When it's surface was added with GA cross-linking,  
316 the  $R_{ct}$  increased. Especially, when ACE2, BSA, and S-protein were added on the  
317 electrode surface, the  $R_{ct}$  values increased orderly due to the non-conductive properties  
318 of these protein layers.

319 To evaluate the electrochemical reaction kinetics of SARS-CoV-2 S-protein at the  
320 BSA/ACE2/GA/ $\text{Fe}_3\text{O}_4@\text{SiO}_2\text{-Au}$ /GCE, different CV curves were measured in  
321 solutions containing 5.0 mmol/L  $[\text{Fe}(\text{CN})_6]^{3-/4-}$  in 0.1 mol/L PBS with a pH 7.0. The  
322 redox peak currents versus the square root of the scan rate curves (Fig. S3) indicate that  
323 the electron transfer process on as-fabricated electrochemical biosensor is diffusion-  
324 controlled [44].

325

### 326 3.3 $\text{Fe}_3\text{O}_4@\text{SiO}_2\text{-Au}$ /GCE sensor optimization

327 In order to obtain the best sensitivity of S-protein detection, the optimization  
328 experiments including the concentration of ACE2, the interaction temperature, and the  
329 interaction time of S-protein and ACE2 (Fig. 6). When the ACE2 is varied between 1  
330 and 25  $\mu\text{g/mL}$ , the  $R_{ct}$  value was optimal at 20  $\mu\text{g/mL}$  ACE2 and afterward, it shows a  
331 slight decline. The system temperature and time exert a significant impact on the  
332 biochemical activity of S-protein. As shown in Fig 6 b & c, optimal  $R_{ct}$  values were  
333 obtained at 37°C interaction temperature and 30 min interaction time. Interestingly it  
334 represents the average body temperature of humans. In subsequent studies, the  
335 following experimental conditions were used; 20  $\mu\text{g/mL}$  ACE2 concentration, 37°C  
336 interaction temperature, and 30 min interaction time.



337

338 Fig. 6. The relationship between charge-transfer resistance signals and the  
 339 concentration of ACE2 (a), the interaction temperature (b), and the interaction time (c)  
 340 of S-protein and ACE2. Error bar = RSD (n = 3).

341

#### 342 3.4 Detection performance of the S-protein electrochemical biosensor

343

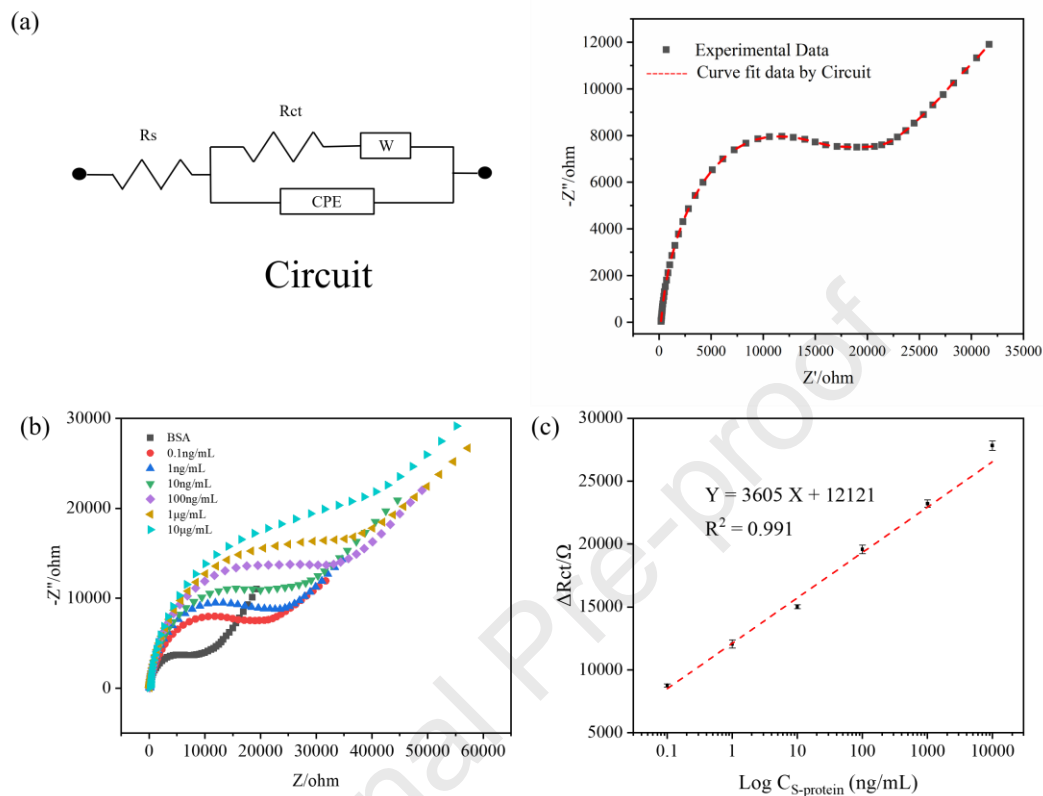
A separate experiment was carried out to determine the performance of the  
 344  $\text{Fe}_3\text{O}_4@\text{SiO}_2\text{-Au/GCE}$  biosensor for S-protein detection as a function of Au  
 345 nanoparticles loading. In this experiment, the loading of Au nanoparticles onto  
 346  $\text{Fe}_3\text{O}_4@\text{SiO}_2$  was varied between 5 mL, 15 mL, 25 mL (Fig. S4). The GCE was then  
 347 chemically modified using  $\text{Fe}_3\text{O}_4@\text{SiO}_2\text{-Au}_x$  where x ranged from 1, 2, 3  
 348 ( $\text{Fe}_3\text{O}_4@\text{SiO}_2\text{-Au}_x/\text{GCE}$ ). The S-protein detection performance obtained by  
 349  $\text{Fe}_3\text{O}_4@\text{SiO}_2\text{-Au}_x/\text{GCE}$  sensor is shown in Fig. S5. Initially, the EIS response signal

350 steadily increased with the Au nanoparticles loading showing an optimal value when  
351  $\text{Fe}_3\text{O}_4@\text{SiO}_2\text{-Au}_2/\text{GCE}$  sensor is used for measurements. At suitable Au nanoparticles  
352 loading, well-dispersed particulates yield an abundance of reactive sites for S-protein  
353 binding. When the Au nanoparticles loading further increased 25mL, the reactivity of  
354 the  $\text{Fe}_3\text{O}_4@\text{SiO}_2\text{-Au}_3/\text{GCE}$  to S-protein is somewhat hindered as a result of particulates  
355 agglomeration (Fig. S5f). Therefore, in optimizing the performance of biosensors for  
356 S-protein detection  $\text{Fe}_3\text{O}_4@\text{SiO}_2\text{-Au}_2/\text{GCE}$  (designated as  $\text{Fe}_3\text{O}_4@\text{SiO}_2\text{-Au}/\text{GCE}$ ) is  
357 used.

358 The EIS response signals of 0.1 ng/mL S-protein solution measured with  
359  $\text{Fe}_3\text{O}_4@\text{SiO}_2\text{-Au}/\text{GCE}$  biosensor were also simulated using a modified Randles  
360 equivalent circuit. Fig. 7a shows the agreement between experimental observations and  
361 the modeled data. The modified Randles model was also used to interpret the Nyquist  
362 plots for a series of S-protein concentrations (0.1 ng/mL to 10  $\mu\text{g}/\text{mL}$ ) (Fig. 7b). The  
363 calculated  $R_{\text{ct}}$  values show a linear dependence with the logarithmic S-protein  
364 concentration when the solution matrix conditions are matched.

365 The relationship between S-protein concentration as a function of  $R_{\text{ct}}$  was  
366 estimated as  $\Delta R_{\text{ct}} = 3605 \text{ Log } C + 12121$  (limit of S-protein detection 4.78 ng/mL;  $R^2$   
367 = 0.991) (Fig 7c). The sensitivity and the linear dynamic range of the SARS-CoV-2 S-  
368 protein determination against our method are compared as shown in Table 1. The  
369 sensitivity and the linear dynamic range of S-protein detection depend on the nature of  
370 the sensors, and the electrochemical method used (for comparison, data obtained by  
371 molecular spectroscopic methods were also given). In terms of sensitivity and the linear

372 dynamic range, the  $\text{Fe}_3\text{O}_4@\text{SiO}_2\text{-Au/GCE}$  sensor developed presently shows the  
 373 highest performance for S-protein detection by the EIS method.



374

375 Fig. 7. (a) The modified Randles circuit with CPE element,  $R_s$  solution resistant, CPE,  
 376 constant phase element,  $R_{ct}$ , charge transfer resistant,  $W$ , Warburg resistant (b)Nyquist  
 377 plots obtained  $\text{Fe}_3\text{O}_4@\text{SiO}_2\text{-Au/GCE}$  at various concentrations of SARS-CoV-2 S-  
 378 protein and (c) the plot of logarithm concentrations against  $\Delta R_{ct}$ .

379 Table 1 The comparison of the performance of biosensors constructed with different  
 380 materials for the detection of SARS-CoV-2 S-protein

Detection	Material	Linear range	LOD	Ref.
SERS	AuNPs	1-5 ng/mL	1 ng/mL	[46]
LIFA	AuNPs	0.1-1 ng/mL	0.1 ng/mL	[47]
Fluorescence	UCNPs@mSiO <sub>2</sub>	2-200 ng/mL	1.6 ng/mL	[48]
MPS	Fe <sub>3</sub> O <sub>4</sub>	2.82-11.26 nM	1.56 nM	[49]
Colorimetric	Au@Pt	10-100 ng/mL	11 ng/mL	[50]
I-t	Co-TNTs	14-1400 nM	0.7 nM	[51]
DPV	SWCNT	0.3-300 nM	7 nM	[52]
LSV	CB/MB	0.04-10 µg/mL	19 ng/mL	[53]
SWV	MB	3.12-200 ng/mL	0.2 ng/mL	[54]
EIS	Fe <sub>3</sub> O <sub>4</sub> @SiO <sub>2</sub> -Au	0.1-10 <sup>4</sup> ng/mL	4.78 pg/mL	This work

381 SERS, Surface-Enhanced Raman Scattering; MPS, magnetic particle spectroscopy; EIS,  
 382 electrochemical impedance spectroscopy; I-t, Amperometry; DPV, Differential Pulse  
 383 Voltammetry; LSV, linear sweep voltammetry; SWV, square wave voltammetry.

384 AuNPs, gold nanoparticles; UCNPs@mSiO<sub>2</sub>, mesoporous silica encapsulated up-  
 385 conversion nanoparticles; Co-TNTs, Co-functionalized TiO<sub>2</sub> nanotubes; SWCNT,  
 386 single-walled carbon nanotube; CB, carbon black; MB, magnetic beads.

387

### 388 *3.5 Selectivity, reproducibility, and repeatability*

389 We examined the selectivity, repeatability, and reproductivity of Fe<sub>3</sub>O<sub>4</sub>@SiO<sub>2</sub>-  
 390 Au/GCE for the detection of S-protein by the EIS method using optimal experimental  
 391 conditions developed in this study. In all these experiments 0.1 ng/mL S-protein  
 392 solution was used. For selectivity analysis glucose, ascorbic acid, BSA, IgG,

393 norfloxacin, uric acid, tenofovir, favipiravir, histidine, oxytetracycline were used as  
394 potential interferants. As shown in Fig. S6a, in the presence of these interferents, the S-  
395 protein in the solution can be detected with high selectivity (RSD < 4%). In evaluating  
396 the sensor reproduction, six identical Fe<sub>3</sub>O<sub>4</sub>@SiO<sub>2</sub>-Au/GCE sensors were fabricated for  
397 S-protein measurements with good reproducibility (Fig. S6b; RSD < 1%). To determine  
398 the repeatability, a newly prepared Fe<sub>3</sub>O<sub>4</sub>@SiO<sub>2</sub>-Au/GCE sensor was used for two  
399 consecutive weeks for measurements of S-protein concentration. The RSD value of S-  
400 protein detection was always less than 5% (Fig. S6c).

401

### 402 3.6 Detection of S-protein in saliva

403 The detection of SARS-CoV-2 S-protein in saliva using Fe<sub>3</sub>O<sub>4</sub>@SiO<sub>2</sub>-Au/GCE  
404 biosensor was also carried out by multiple standard addition method. The filtered and  
405 diluted saliva sample was spiked with S-protein at varying concentrations between 1  
406 and 100 ng/mL, and the final analyte concentration was determined in triplicate by EIS;  
407 the results thus obtained are given in Table 2. The spiked recovery of S-protein in the  
408 saliva is always above 97% and the relative standard deviation is below 5%. The results  
409 indicate the suitability of Fe<sub>3</sub>O<sub>4</sub>@SiO<sub>2</sub>-Au/GCE biosensor in detecting SARS-CoV-2  
410 S-protein in saliva with high precision and accuracy.

411

412 Table 2 Detection of S-protein in real saliva samples

Samples	S-protein concentration (ng/mL)	Recovered (ng/mL)	Recovery(%)	RSD(%)
1	1	1.03	103	4.1
2	5	4.94	98.8	3.2
3	10	9.71	97.1	3.6
4	50	49.7	99.4	4.4
5	100	102	102	3.5

413

414 **4. Conclusions**

415 Preventing the spread of the SARS-CoV-2 virus and its variants requires the  
416 development of a rapid and cost-effective detection method. To our knowledge for the  
417 first time, we developed an electrochemical sensor by chemically modifying a GCE  
418 with Fe<sub>3</sub>O<sub>4</sub>@SiO<sub>2</sub>-Au (Fe<sub>3</sub>O<sub>4</sub>@SiO<sub>2</sub>-Au/GCE) for rapid detection of SARS-CoV-2 S-  
419 protein with a wide dynamic range (0.1 ng/mL to 10 µg/mL) and low limit detection  
420 (4.78 pg/mL). The new electrochemical sensor shows robust behavior with excellent  
421 stability and reproducibility for S-protein detection. Moreover, the sensor could  
422 ultimately lead to corresponding determination in real samples. Once a miniaturized  
423 module of the electrochemical sensor is fabricated (currently in progress), it holds  
424 promise as a sensitive screening method to combat the SARS-CoV-2 global endemic.

425

426 **5. Acknowledgments**

427 The authors acknowledge the financial support from the National Key Research  
428 and Development Program of China (Grant No. 2022YFE0110100), Key Science and  
429 Technology Projects of Anhui Province (Grant No. 202003a07020004), and National

430 Natural Science Foundation of China (No. 21777164). Program of Distinguished  
431 Professor in B & R Countries (Grant No. DL20180052) abidance at the Hefei  
432 University of Technology.

### 433 **References**

- 434 [1] M. Cevik, M. Tate, O. Lloyd, A.E. Maraolo, J. Schafers, A. Ho, SARS-CoV-2, SARS-CoV, and  
435 MERS-CoV viral load dynamics, duration of viral shedding, and infectiousness: a systematic review and  
436 meta-analysis, *Lancet Microbe*. 2 (2021) 13-22. [https://doi.org/10.1016/s2666-5247\(20\)30172-5](https://doi.org/10.1016/s2666-5247(20)30172-5).
- 437 [2] K. Dhama, S. Khan, R. Tiwari, S. Sircar, S. Bhat, Y.S. Malik, K.P. Singh, W. Chaicumpa, D.K.  
438 Bonilla-Aldana, A.J. Rodriguez-Morales, Coronavirus Disease 2019-COVID-19, *Clinical Microbiology*  
439 *Reviews*. 33 (2020) e00028-20. <https://doi.org/10.1128/cmr.00028-20>.
- 440 [3] R. Antiochia, Nanobiosensors as new diagnostic tools for SARS, MERS and COVID-19: from past  
441 to perspectives, *Microchimica Acta*. 187 (2020) 639. <https://doi.org/10.1007/s00604-020-04615-x>.
- 442 [4] Y.W. Tang, J.E. Schmitz, D.H. Persing, C.W. Stratton, Laboratory Diagnosis of COVID-19: Current  
443 Issues and Challenges, *Journal of Clinical Microbiology*. 58 (2020) e00512-20.  
444 <https://doi.org/10.1128/jcm.00512-20>.
- 445 [5] M. Li, F.F. Yin, L. Song, X.H. Mao, F. Li, C.H. Fan, X.L. Zuo, Q. Xia, Nucleic Acid Tests for Clinical  
446 Translation, *Chemical Reviews*. 121 (2021) 10469-10558. <https://doi.org/10.1021/acs.chemrev.1c00241>.
- 447 [6] D.C. Lin, L. Liu, M.X. Zhang, Y.L. Hu, Q.T. Yang, J.B. Guo, Y.C. Dai, Y.Z. Xu, Y. Cai, X.C. Chen,  
448 K.S. Huang, Z. Zhang, Evaluations of the serological test in the diagnosis of 2019 novel coronavirus  
449 (SARS-CoV-2) infections during the COVID-19 outbreak, *European Journal of Clinical Microbiology*  
450 *& Infectious Diseases*. 39 (2020) 2271-2277. <https://doi.org/10.1007/s10096-020-03978-6>.
- 451 [7] Y. Dang, N. Liu, C.A.R. Tan, Y.M. Feng, X.X. Yuan, D.D. Fan, Y.K. Peng, R.H. Jin, Y. Guo, J.L. Lou,  
452 Comparison of qualitative and quantitative analyses of COVID-19 clinical samples, *Clinica Chimica*  
453 *Acta*. 510 (2020) 613-616. <https://doi.org/10.1016/j.cca.2020.08.033>.
- 454 [8] Z. Abusrewil, I.M. Alhudiri, H.H. Kaal, S.E. El Meshri, F.O. Ebrahim, T. Dalyoum, A.A. Efrefer, K.  
455 Ibrahim, M.B. Elfghi, S. Abusrewil, A. Elzagheid, Time scale performance of rapid antigen testing for  
456 SARS-CoV-2: Evaluation of 10 rapid antigen assays, *Journal of Medical Virology*. 93 (2021) 6512-6518.  
457 <https://doi.org/10.1002/jmv.27186>.
- 458 [9] Z.H. Chen, Z.G. Zhang, X.M. Zhai, Y.Y. Li, L. Lin, H. Zhao, L. Bian, P. Li, L. Yu, Y.S. Wu, G.F. Lin,  
459 Rapid and Sensitive Detection of anti-SARS-CoV-2 IgG, Using Lanthanide-Doped Nanoparticles-Based  
460 Lateral Flow Immunoassay, *Analytical Chemistry*. 92 (2020) 7226-7231.  
461 <https://doi.org/10.1021/acs.analchem.0c00784>.
- 462 [10] X. Pan, A.C. Kaminga, Y. Chen, H. Liu, S.W. Wen, Y. Fang, P. Jia, A. Liu, Auxiliary Screening  
463 COVID-19 by Serology, *Frontiers in Public Health*. 10 (2022).  
464 <https://doi.org/10.3389/fpubh.2022.819841>.
- 465 [11] B. Li, A.M. Yu, G.S. Lai, Self-assembly of phenoxy-dextran on electrochemically reduced graphene  
466 oxide for nonenzymatic biosensing of glucose, *Carbon*. 127 (2018) 202-208.  
467 <https://doi.org/10.1016/j.carbon.2017.10.096>.
- 468 [12] M. Negahdary, L. Angnes, Electrochemical aptamer-based nanobiosensors for diagnosing  
469 Alzheimer's disease: A review, *Biomaterials Advances*. 135 (2022) 112689.  
470 <https://doi.org/10.1016/j.msec.2022.112689>.

- 471 [13] L.J. Lei, B. Ma, C.T. Xu, H. Liu, Emerging tumor-on-chips with electrochemical biosensors, *Trac-*  
472 *Trends in Analytical Chemistry*. 153 (2022) 116640. <https://doi.org/10.1016/j.trac.2022.116640>.
- 473 [14] T. Chaibun, J. Puenpa, T. Ngamdee, N. Boonapatcharoen, P. Athamanolap, A.P. O'Mullane, S.  
474 Vongpunsawad, Y. Poovorawan, S.Y. Lee, B. Lertanantawong, Rapid electrochemical detection of  
475 coronavirus SARS-CoV-2, *Nature Communications*. 12 (2021) 802. [https://doi.org/10.1038/s41467-021-](https://doi.org/10.1038/s41467-021-21121-7)  
476 [21121-7](https://doi.org/10.1038/s41467-021-21121-7).
- 477 [15] J. Kudr, P. Michalek, L. Ilieva, V. Adam, O. Zitka, COVID-19: a challenge for electrochemical  
478 biosensors, *TrAC Trends in Analytical Chemistry*. 136 (2021) 116192.  
479 <https://doi.org/10.1016/j.trac.2021.116192>.
- 480 [16] V.V. Tran, N.H.T. Tran, H.S. Hwang, M. Chang, Development strategies of conducting polymer-  
481 based electrochemical biosensors for virus biomarkers: Potential for rapid COVID-19 detection,  
482 *Biosensors & Bioelectronics*. 182 (2021) 540-552. <https://doi.org/10.1016/j.bios.2021.113192>.
- 483 [17] A. Gb, B. Aba, A. Ma, B. Np, C. Ss, E. Ptad, Emerging materials for the electrochemical detection  
484 of COVID-19, *Journal of Electroanalytical Chemistry*. 893 (2021) 115289.  
485 <http://doi.org/10.1016/j.jelechem.2021.115289>.
- 486 [18] M. Elbadawi, J.J. Ong, T.D. Pollard, S. Gaisford, A.W. Basit, Additive Manufacturable Materials  
487 for Electrochemical Biosensor Electrodes, *Advanced Functional Materials*. 31 (2021) 2006407.  
488 <https://doi.org/10.1002/adfm.202006407>.
- 489 [19] A.L. Lorenzen, A.M. Dos Santos, L.P. Dos Santos, L. da Silva Pinto, F.R. Conceicao, F. Wolfart,  
490 PEDOT-AuNPs-based impedimetric immunosensor for the detection of SARS-CoV-2 antibodies,  
491 *Electrochimica acta*. 404 (2022) 139757-139757. <https://doi.org/10.1016/j.electacta.2021.139757>.
- 492 [20] M.A. Ali, C. Hu, S. Jahan, B. Yuan, M.S. Saleh, E. Ju, S.-J. Gao, R. Panat, Sensing of COVID-19  
493 Antibodies in Seconds via Aerosol Jet Nanoprinted Reduced-Graphene-Oxide-Coated 3D Electrodes,  
494 *Advanced Materials*. 33 (2021) 2006647. <https://doi.org/10.1002/adma.202006647>.
- 495 [21] R. Torrente-Rodríguez, H. Lukas, J. Tu, J. Min, Y. Yang, C. Xu, H.B. Rossiter, W. Gao, SARS-CoV-  
496 2 RapidPlex: A Graphene-Based Multiplexed Telemedicine Platform for Rapid and Low-Cost COVID-  
497 19 Diagnosis and Monitoring, *Matter*. 3 (2020) 1981-1998. <https://doi.org/10.1016/j.matt.2020.09.027>.
- 498 [22] F. Haghayegh, R. Salahandish, M. Hassani, A. Sanatinezhad, Highly Stable Buffer-Based Zinc  
499 Oxide/Reduced Graphene Oxide Nanosurface Chemistry for Rapid Immunosensing of SARS-CoV-2  
500 Antigens, *ACS Applied Materials & Interfaces*. 14 (2022) 10844-10855. [https://doi.org/](https://doi.org/10.1021/acsami.1c24475)  
501 [10.1021/acsami.1c24475](https://doi.org/10.1021/acsami.1c24475).
- 502 [23] H.V. Tran, N.M. Ngo, R. Medhi, P. Srinoi, T.T. Liu, S. Rittikulsittichai, T.R. Lee, Multifunctional  
503 Iron Oxide Magnetic Nanoparticles for Biomedical Applications: A Review, *Materials*. 15 (2022) 503.  
504 <https://doi.org/10.3390/ma15020503>.
- 505 [24] N. Sanaeifar, M. Rabiee, M. Abdolrahim, M. Tahriri, D. Vashae, L. Tayebi, A novel electrochemical  
506 biosensor based on Fe<sub>3</sub>O<sub>4</sub> nanoparticles-polyvinyl alcohol composite for sensitive detection of glucose,  
507 *Analytical Biochemistry*. 519 (2017) 19-26. <https://doi.org/10.1016/j.ab.2016.12.006>.
- 508 [25] X.N. Liu, F.H. Zhu, W. Wang, J.H. Lei, G.F. Yin, Synthesis of Single-Crystalline Iron Oxide  
509 Magnetic Nanorings as Electrochemical Biosensor for Dopamine Detection, *International Journal of*  
510 *Electrochemical Science*. 11 (2016) 9696-9703. <https://doi.org/10.20964/2016.11.62>.
- 511 [26] R. Antiochia, Electrochemical biosensors for SARS-CoV-2 detection: Voltametric or impedimetric  
512 transduction?, *Bioelectrochemistry*. 147 (2022) 108190.  
513 <https://doi.org/10.1016/j.bioelechem.2022.108190>.
- 514 [27] M. Torres, W. Araujo, L. Lima, A.L. Ferreira, C. Fuente-Nunez, Low-cost biosensor for rapid

- 515 detection of SARS-CoV-2 at the point of care, *Matter*, 4 (2021) 2403-2416.  
516 <https://doi.org/10.1016/j.matt.2021.05.003>.
- 517 [28] Y.T. Buyuksunetci, B.E. Cital, U. Anik, An impedimetric approach for COVID-19 detection, *Analyst*.  
518 147 (2021) 130-138. <https://doi.org/10.1039/d1an01718g>.
- 519 [29] Z. Lukacs, T. Kristof, A generalized model of the equivalent circuits in the electrochemical  
520 impedance spectroscopy, *Electrochimica Acta*. 363 (2020).  
521 <https://doi.org/10.1016/j.electacta.2020.137199>.
- 522 [30] J. Liu, Z.K. Sun, Y.H. Deng, Y. Zou, C.Y. Li, X.H. Guo, L.Q. Xiong, Y. Gao, F.Y. Li, D.Y. Zhao,  
523 Highly Water-Dispersible Biocompatible Magnetite Particles with Low Cytotoxicity Stabilized by  
524 Citrate Groups, *Angewandte Chemie-International Edition*. 48 (2009) 5875-5879.  
525 <https://doi.org/10.1002/anie.200901566>.
- 526 [31] C. Hui, C.M. Shen, J.F. Tian, L.H. Bao, H. Ding, C. Li, Y.A. Tian, X.Z. Shi, H.J. Gao, Core-shell  
527  $\text{Fe}_3\text{O}_4@/\text{SiO}_2$  nanoparticles synthesized with well-dispersed hydrophilic  $\text{Fe}_3\text{O}_4$  seeds, *Nanoscale*. 3 (2011)  
528 701-705. <https://doi.org/10.1039/c0nr00497a>.
- 529 [32] K.R. Brown, A.P. Fox, M.J. Natan, Morphology-Dependent Electrochemistry of Cytochrome c at  
530 Au Colloid-Modified  $\text{SnO}_2$  Electrodes, *Journal of the American Chemical Society*. 118 (1996) 1154-1157.  
531 <https://doi.org/10.1021/ja952951w>.
- 532 [33] H. Deng, X.L. Li, Q. Peng, X. Wang, J.P. Chen, Y.D. Li, Monodisperse magnetic single-crystal  
533 ferrite microspheres, *Angewandte Chemie-International Edition*. 44 (2005) 2782-2785.  
534 <https://doi.org/10.1002/anie.200462551>.
- 535 [34] Q. Zhang, R. Chen, J.Y. Gong, M. Yuan, L.Y. Chen, Single-crystalline  $\text{Fe}_3\text{O}_4$  nanosheets: Facile  
536 sonochemical synthesis, evaluation and magnetic properties, *Journal of Alloys and Compounds*. 577  
537 (2013) 528-532. <https://doi.org/10.1016/j.jallcom.2013.06.176>.
- 538 [35] W. Zhang, F.L. Shen, R.Y. Hong, Solvothermal synthesis of magnetic  $\text{Fe}_3\text{O}_4$  microparticles via self-  
539 assembly of  $\text{Fe}_3\text{O}_4$  nanoparticles, *Particuology*. 9 (2011) 179-186.  
540 <https://doi.org/10.1016/j.partic.2010.07.025>.
- 541 [36] N. Shahabadi, M. Falsafi, K. Mansouri, Improving antiproliferative effect of the anticancer drug  
542 cytarabine on human promyelocytic leukemia cells by coating on  $\text{Fe}_3\text{O}_4@/\text{SiO}_2$  nanoparticles, *Colloids*  
543 *and Surfaces B-Biointerfaces*. 141 (2016) 213-222. <https://doi.org/10.1016/j.colsurfb.2016.01.054>.
- 544 [37] M.E. Khosroshahi, L. Ghazanfari, Physicochemical characterization of  $\text{Fe}_3\text{O}_4/\text{SiO}_2/\text{Au}$  multilayer  
545 nanostructure, *Materials Chemistry and Physics*. 133 (2012) 55-62.  
546 <https://doi.org/10.1016/j.matchemphys.2011.12.047>.
- 547 [38] T. Radu, A. Petran, D. Olteanu, I. Baldea, M. Potara, R. Turcu, Evaluation of physico-chemical  
548 properties and biocompatibility of new surface functionalized  $\text{Fe}_3\text{O}_4$  clusters of nanoparticles, *Applied*  
549 *Surface Science*. 501 (2020) 144267. <https://doi.org/10.1016/j.apsusc.2019.144267>.
- 550 [39] M.C. Biesinger, B.P. Payne, A.P. Grosvenor, L.W.M. Lau, A.R. Gerson, R.S. Smart, Resolving  
551 surface chemical states in XPS analysis of first row transition metals, oxides and hydroxides: Cr, Mn, Fe,  
552 Co and Ni, *Applied Surface Science*. 257 (2011) 2717-2730.  
553 <https://doi.org/10.1016/j.apsusc.2010.10.051>.
- 554 [40] T. Paixao, Measuring electrochemical surface area of nanomaterials versus Randles-Ševčík equation,  
555 *ChemElectroChem*. 7 (2020) 3414-3415. <https://doi.org/10.1002/celec.202000633>.
- 556 [41] V. Vivier, M.E. Orazem, Impedance Analysis of Electrochemical Systems, *Chemical Reviews*. 122  
557 (2022) 11131-11168. <https://doi.org/10.1021/acs.chemrev.1c00876>.
- 558 [42] O. Gharbi, M.T.T. Tran, B. Tribollet, M. Turmine, V. Vivier, Revisiting cyclic voltammetry and

- 559 electrochemical impedance spectroscopy analysis for capacitance measurements, *Electrochimica Acta*.  
560 343 (2020) 136109. <https://doi.org/10.1016/j.electacta.2020.136109>.
- 561 [43] C.M.A. Brett, *Electrochemical Impedance Spectroscopy in the Characterisation and Application of*  
562 *Modified Electrodes for Electrochemical Sensors and Biosensors*, *Molecules*. 27 (2022) 1497.  
563 <https://doi.org/10.3390/molecules27051497>.
- 564 [44] M. Mehmandoust, S. Cakar, M. Ozacar, N. Erk, The Determination of Timolol Maleate Using  
565 Silver/Tannic Acid/Titanium Oxide Nanocomposite as an Electrochemical Sensor in Real Samples,  
566 *Electroanalysis*. 34 (2022) 1150-1162. <https://doi.org/10.1002/elan.202100363>.
- 567 [45] R. Saxena, S. Srivastava, An insight into impedimetric immunosensor and its electrical equivalent  
568 circuit, *Sensors and Actuators B-Chemical*. 297 (2019) 126780.  
569 <https://doi.org/10.1016/j.snb.2019.126780>.
- 570 [46] A. Pramanik, Y. Gao, S. Patibandla, D. Mitra, P.C. Ray, Rapid Diagnosis and Effective Inhibition of  
571 Corona Virus Using Spike Antibody Attached Gold Nanoparticle, *Nanoscale Advances*. 3 (2021) 1588-  
572 1596. <https://doi.org/10.1039/d0na01007c>.
- 573 [47] K.V. Serebrennikova, N.A. Byzova, A.V. Zherdev, N.G. Khlebtsov, B.N. Khlebtsov, S.F. Biketov,  
574 B.B. Dzantiev, Lateral Flow Immunoassay of SARS-CoV-2 Antigen with SERS-Based Registration:  
575 Development and Comparison with Traditional Immunoassays, *Biosensors*. 11 (2021) 510.  
576 <https://doi.org/10.3390/bios11120510>.
- 577 [48] J. Guo, 5G-Enabled Ultra-Sensitive Fluorescence Sensor for Proactive Prognosis of COVID-19,  
578 *Biosensors & Bioelectronics*. (2020) 113160. <https://doi.org/10.1016/j.bios.2021.113160>.
- 579 [49] K. Wu, V.K. Chugh, V.D. Krishna, A.D. Girolamo, Y.A. Wang, R. Saha, S. Liang, C.J. Cheeran, J.P.  
580 Wang, One-step, Wash-free, Nanoparticle Clustering-based Magnetic Particle Spectroscopy (MPS)  
581 Bioassay Method for Detection of SARS-CoV-2 Spike and Nucleocapsid Proteins in Liquid Phase, *ACS*  
582 *Applied Materials & Interfaces*, 13 (2021) 44136-44146. <https://doi.org/10.1021/acsami.1c14657>.
- 583 [50] Z. Fu, W. Zeng, S. Cai, H. Li, R. Yang, Porous Au@Pt nanoparticles with superior peroxidase-like  
584 activity for colorimetric detection of spike protein of SARS-CoV-2, *Journal of Colloid and Interface*  
585 *Science*. 604 (2021) 113-121. <https://doi.org/10.1016/j.jcis.2021.06.170>.
- 586 [51] B.S. Vadlamani, T. Uppal, S.C. Verma, M. Misra, Functionalized TiO<sub>2</sub> Nanotube-Based  
587 Electrochemical Biosensor for Rapid Detection of SARS-CoV-2, *Sensors*. 20 (2020) 5871.  
588 <https://doi.org/10.1101/2020.09.07.20190173>.
- 589 [52] F. Curti, S. Fortunati, W. Knoll, M. Giannetto, R. Corradini, A. Bertucci, M. Careri, A Folding-Based  
590 Electrochemical Aptasensor for the Single-Step Detection of the SARS-CoV-2 Spike Protein, *ACS*  
591 *Applied Materials & Interfaces*. 14 (2022) 19204-19211. <https://doi.org/10.1021/acsami.2c02405>.
- 592 [53] L. Fabiani, M. Saroglia, G. Galatà, R.D. Santis, F. Arduini, Magnetic beads combined with carbon  
593 black-based screen-printed electrodes for COVID-19: A reliable and miniaturized electrochemical  
594 immunosensor for SARS-CoV-2 detection in saliva, *Biosensors & Bioelectronics*. 171 (2021) 112686.  
595 <https://doi.org/10.1016/j.bios.2020.112686>.
- 596 [54] P. Malla, H.P. Liao, C.H. Liu, W.C. Wu, P. Sreearunothai, Voltammetric biosensor for coronavirus  
597 spike protein using magnetic bead and screen-printed electrode for point-of-care diagnostics,  
598 *Microchimica Acta*. 189 (2022) 168. <https://doi.org/10.1016/j.bios.2020.112686>.
- 599

**Declaration of interests**

The authors declare that they have no known competing financial interests or personal relationships that could have appeared to influence the work reported in this paper.

The authors declare the following financial interests/personal relationships which may be considered as potential competing interests:

Journal Pre-proof